One-dimensional pattern of Au nanodots by ion-beam sputtering: formation and mechanism

2011 Nanotechnology 22 285301

(http://iopscience.iop.org/0957-4484/22/28/285301)

Nanotechnology **22** (2011) 285301 (8pp) doi:10.1088/0957-4484/22/28/285301

One-dimensional pattern of Au nanodots by ion-beam sputtering: formation and mechanism

J-H Kim[1], N-B Ha[1], J-S Kim[1], M Joe[2], K-R Lee[2] and R Cuerno[3]

[1] Department of Physics, Sook-Myung Women's University, Seoul 140-742, Korea
[2] Computational Science Center, Korea Institute of Science and Technology, Seoul 136-791, Korea
[3] Departamento de Matemáticas and Grupo Interdisciplinar de Sistemas Complejos (GISC), Universidad Carlos III de Madrid, Avenida de la Universidad 30, E-28911 Leganés, Spain

E-mail: jskim@sm.ac.kr

Received 13 January 2011, in final form 6 April 2011
Published 31 May 2011
Online at stacks.iop.org/Nano/22/285301

Abstract
Highly ordered one-dimensional arrays of nanodots, or nanobeads, are fabricated by forming nanoripples and nanodots in sequence, entirely by ion-beam sputtering (IBS) of Au(001). This demonstrates the capability of IBS for the fabrication of sophisticated nanostructures via hierarchical self-assembly. The intricate nanobead pattern ideally serves to identify the governing mechanisms for the pattern formation: nonlinear effects, especially local redeposition and surface-confined transport, are essential both for the formation and the preservation of the one-dimensional order of the nanobead pattern.

(Some figures in this article are in colour only in the electronic version)

1. Introduction

Ion-beam sputtering (IBS) has stimulated extensive experimental and theoretical studies due to its potential to fabricate ordered nanopatterns on many different surfaces in a self-organized fashion [1, 2]. Nanopatterning by IBS can be universally applied to various materials ranging from metals [3], semiconductors [4], oxides [5] to polymers [6, 7]. Thus, patterned surfaces show novel catalytic [8], magnetic [9, 10], and optical properties [11], facilitating the functionalization of various surfaces.

Although a full microscopic understanding of pattern formation by IBS has not been achieved yet (see e.g. the recent special issue devoted to this topic in [12]), the typical length scale characterizing the ensuing pattern needs to emerge from the competition between destabilizing mechanisms that amplify initial height deviations from a flat interface, and competing, smoothening mechanisms [13]. It is widely agreed that the former mechanisms are induced by the ion beam, the latter being associated with material transport effects, such as surface diffusion. For instance, in the classic description by Bradley and Harper [14], built upon Sigmund's linear cascade description of collision cascades [15], the local rate of erosion at a surface point is proportional to the average energy deposited there due to the slowing down of the incoming ions through collisions with the target atoms within a surface region a few nanometers across (ion range). The local sputter yield turns out to be larger at surface minima [15], where energy deposition is 'focalized', than at surface maxima. This results into a morphological instability, since minima erode faster than maxima and initial height inhomogeneities are amplified. At the same time, smoothening occurs by surface diffusion of sputter-induced adatoms and vacancies [16]. The competition between these two processes results in the formation of a periodic pattern with a typical scale that is usually larger than the ion range [1, 2].

Notwithstanding the wide generality of the previous pattern formation mechanism, the structures produced by IBS are essentially restricted to periodic ripples and nanohole/dot arrays, that are generated respectively by oblique and normal beam incidence onto the target surface. With a few exceptions such as IBS with a rotating substrate [17] and with an angularly dispersed ion beam [18], most sputter-induced patterns have been fabricated simply by a single ion beam in a single sputter geometry. Such a practice seems to limit the diversity of the patterns produced. To overcome this limitation, recently

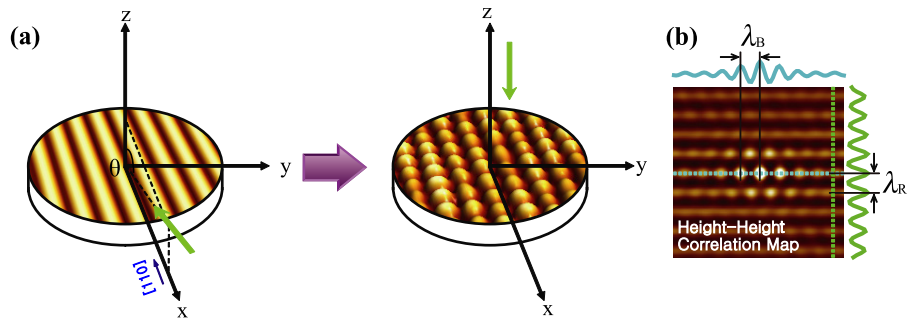

Figure 1. (a) Schematic illustration of the experimental geometry for the fabrication of nanobead patterns by sequential-ion-beam sputtering (SIBS) on Au(001) substrate. (b) Schematic illustration showing how the mean wavelength of ripple λ_R and mean wavelength of bead λ_B are retrieved from the 2D height–height correlation map. The employed images are obtained from a numerical simulation starting from a uniform ripple pattern.

multiple-ion-beam sputtering has been proposed to produce diverse arrangements via interference of patterns formed by several ion beams. Within one approach, more than two ion beams are projected onto a surface simultaneously from different orientations [19–21]. Actually, some of us demonstrated that square symmetric patterns of nanoholes and nanodots can be fabricated on Au(001) by dual-ion-beam sputtering even at oblique incidence [22]. Another approach is sequential-ion-beam sputtering (SIBS) of a surface, where different ion beams are employed sequentially, changing their orientation with respect to the substrate [21]. To examine this possibility, Kim *et al* [23] first formed a ripple pattern in one direction by sputtering at a grazing angle, and sputtered the surface subsequently changing only the azimuthal angle by 90°. The resulting pattern is, however, not the one made by the mere superposition of the crossing ripples, which contradicts previous theoretical predictions [21]. Recently, SIBS has also proven effective in the improvement of the order of ripple patterns [24].

In this work, we present yet another realization of SIBS that is aimed at diversifying the available nanopatterns in a controlled manner. We first fabricate a ripple pattern on Au(001) by IBS at an oblique incidence angle, and then sputter that rippled surface at normal incidence. Highly ordered nanodots form selectively on the pre-patterned ripples. We call this salient one-dimensional (1D) feature, nanobead pattern. Again, this pattern negates the idea of solid phase superposition of patterns formed by each beam [21]. Instead, the nanobead pattern demonstrates the potential of SIBS to fabricate sophisticated ordered nanostructures by sequential fabrication of simple structures, in a so-called hierarchical self-assembly. Note that, up to now, hierarchical self-assembly by IBS had been always guided by ordered templates previously patterned by top-down approaches such as lithography [25] and focused ion beams [26]. The present work proceeds, instead, via a fully bottom-up approach. This novel scheme for hierarchical self-assembly might thus overcome well-known limits imposed by the top-down fabrication of templates such as high cost, low processing speed, and limited template material and patterned area.

To understand how the nanobead patterns develop by SIBS, we have performed an extensive numerical study that is based on the models that are to date best established in the context of nanostructuring by IBS [2]. The nanobead structure serves as a test bed for model assessment, since for each model the ensuing pattern depends sensitively on the underlying physical processes that are considered, like curvature dependent sputtering yield, irradiation-induced transport, surface diffusion, etc. Agreement between experiments and numerical simulations suggests that nonlinear effects, especially local redeposition effects, play a crucial role in the evolution of 1D ordering of the nanobead pattern. Actually, the significant role of redeposition has been already observed for highly corrugated surfaces [22, 23, 27].

2. Experiment

Figure 1(a) shows a schematic of the fabrication of nanobead patterns on Au(001) by two steps in sequence. In the first step, ripple patterns are produced by Ar^+ beam sputtering of Au(001) (purity 99.999%, Mateck) along the densely packed [110] direction with a polar angle $\theta = 72°$ from the surface normal. After fabricating the initial ripple patterns, we further sputter the rippled surface at normal incidence.

For the formation of initial ripple patterns, the partial pressure of Ar^+ P_{Ar}, the ion energy ε, the ion flux f, and the ion fluence ψ were 1.2×10^{-4} Torr, 2 keV, 0.3 ions nm^{-2} s^{-1}, and 4500 ions nm^{-2}, respectively. The ion fluence is defined as the ion flux multiplied by the accumulated sputter time. This sputter condition corresponds to the erosive regime in which the sputter erosion plays the major role in the pattern formation compared with the diffusion of adspecies [23]. The ripple pattern is better defined with less defects in the erosive regime, since the perturbation during the pattern formation via diffusion of adspecies is weaker in the erosive regime than in the diffusive regime [23].

For the subsequent sputtering at normal incidence, P_{Ar}, ε, and f were 1.2×10^{-4} Torr, 2 keV, and 1.1875 ions nm^{-2} s^{-1}, respectively. For the present choice of the fluxes, the mean wavelength of ripple λ_R is similar to the mean nanodot diameter formed by the sputtering normal to a flat surface in the asymptotic regime. In this case, we obtain the highest quality of nanobead pattern with the least defect density [28].

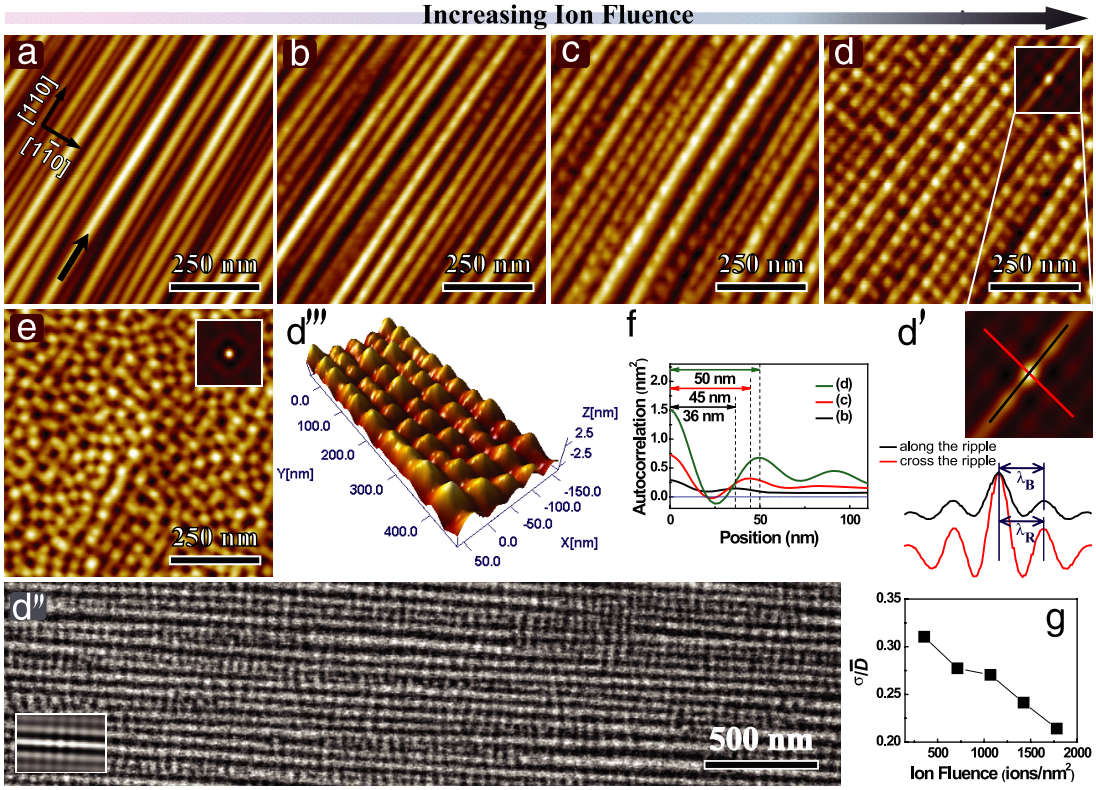

Figure 2. (a)–(e) AFM images. (a) Initial, rippled surface with $\lambda_R \simeq 47$ nm and $W \simeq 2.7$ nm. The arrow indicates the incidence direction of the ion beam as projected onto the target plane. Surface morphologies after sputtering normal to the rippled surface with (b) $\psi = 356$ ions nm^{-2}, (c) $\psi = 1069$ ions nm^{-2} and (d) $\psi = 1781$ ions nm^{-2}. (e) Surface morphology after sputtering normal to an initially flat surface with $\psi = 1781$ ions nm^{-2}. The insets are 2D height–height correlation maps. (d′) Line profiles both along and across the ripple in the zoomed in image of the inset of (d). This demonstrates how λ_B and λ_R are obtained. (d″) SEM image of the sample giving the image (d). (d‴) 3D image of the ordered nanobead pattern of the sample (d). (f) 1D height–height correlation functions along the ripple for (b)–(d). The distance from the zeroth peak to the first peak denotes λ_B. λ_Bs are estimated to $\simeq$36 nm, $\simeq$45 nm and $\simeq$50 nm for (b)–(d), respectively. (g) Evolution of $\sigma/\bar{D}$, where σ is the standard deviation of the distribution of the nanobead diameter D. Image size: ((a)–(e)) 750 × 750 nm^2 and (d″) 3600 × 880 nm^2.

All the experiments for the sample sputtering were performed in a custom-built ultrahigh vacuum chamber with a base pressure of about 5×10^{-10} Torr. Ar ions were generated by using a commercial ion gun (Perkin Elmer, 20-045). During the sputtering, the sample temperature was kept around 300 K. The patterned surface was then analyzed *ex situ* by an atomic force microscope (AFM, PSI, Autoprobe CP) in the contact mode and a scanning electron microscope (SEM, Hitachi, S-4300).

From the AFM images of the nanobead pattern, we retrieve the following structural information: the surface roughness W is defined as $W(t) \equiv \sqrt{\langle [h(\mathbf{r},t) - \bar{h}(t)]^2 \rangle}$, where $\bar{h}(t)$ is the mean height at time t. The mean ripple wavelength $\lambda_R(t)$ and mean nanobead wavelength $\lambda_B(t)$ are obtained from the two-dimensional (2D) height–height correlation function $G(\mathbf{r})$ of AFM images as illustrated in figure 1(b). Here, $G(\mathbf{r})$ is defined as $G(\mathbf{r}) \equiv \langle h(\mathbf{r} + \mathbf{r}_i) h(\mathbf{r}_i) \rangle$, with λ_R being estimated as the distance between the central ripple and the neighboring ones from a 2D map of $G(\mathbf{r})$. Finally, λ_B is obtained from the line profiles along the central ripples of the 2D map of $G(\mathbf{r})$. Due to the compact arrangement of beads along each ripple, λ_B can be interpreted as the mean diameter $\bar{D}$ of the nanobeads.

For the case of an immature nanobead pattern, however, it is hard to measure λ_B from the 2D map of $G(\mathbf{r})$, because nanobeads do not extend along whole ripple length and the height modulation of the beads (along the ripple) is smaller than that of the ripple (across the ripple). Thus, we obtain a 1D height–height correlation function from the line profiles along the ripple where nanobeads develop, and obtain λ_B from it.

3. Results

Figure 2(a) shows a typical ripple pattern formed after sputtering at an oblique angle $\theta = 72°$. For this structure, λ_R and W are 47 nm and 2.7 nm, respectively. The ripples form along the direction of the incident ion beam, that is chosen to coincide with the densely packed crystallographic direction [110]. Figures 2(b)–(d) illustrate the development of the nanobead patterns upon the initial ripples by subsequent ion-beam sputtering at normal incidence with increasing ion fluence ψ.

At an ion fluence $\psi = 356$ ions nm^{-2} (figure 2(b)), we can observe that nanobeads sporadically develop along the initial ripple, with $\lambda_B \simeq 36$ nm and $A_B \simeq 0.5$ nm. At an ion fluence $\psi = 1069$ ions nm^{-2}, nanobeads are found to cover most

of the top area of the ripples (figure 2(c)). Now λ_B and A_B increase to 45 nm and 0.8 nm, respectively. Both λ_B and A_B are retrieved from the 1D height–height correlation function as shown in figure 2(f).

With a further increase of ion fluence $\psi = 1781$ ions nm^{-2}, we can observe well-ordered nanobeads over the whole top area (figure 2(d)). Each bead has grown further with $\lambda_B \simeq 50$ nm and $A_B \simeq 1.2$ nm. A_B are obtained from the 1D height–height correlation function in figure 2(f), while both λ_B and λ_R are obtained from the 2D height–height correlation map as shown in figure 2(d′) (λ_Bs obtained from both 1D and 2D height–height correlation functions are found to be the same). Figure 2(d″) is the image of the same sample taken by a SEM that gives a wider areal view. The image shows the nanobead pattern to extend over the whole ripple length, longer than 3 μm.

Figure 2(g) shows that the standard deviation of the nanobead size distribution, normalized by the mean bead diameter or mean bead wavelength, $\sigma/\bar{D}$, also decreases with increasing ψ, from 0.31 for figure 2(a) down to a minimal value, 0.21 for figure 2(d). This indicates that as sputtering proceeds, the nanobead size becomes more and more uniform.

The height–height correlation functions $G(\mathbf{r})$ of the nanobead patterns of figures 2(d) and (d″) are displayed in the inset of each figure. A square symmetric pattern is observed around the central peak, implying that the nanobeads are well ordered not only along the ripple direction [110], but also along the inter-ripple direction [1$\bar{1}$0], although the inter-ripple correlation of the beads is weak relative to the intra-ripple correlation. Such an order between the beads on adjacent ripples indicates that adatoms generated by the normal incidence irradiation can efficiently diffuse along the close packed [1$\bar{1}$0] direction that is perpendicular to the ripples, and mediate the correlated growth of the beads in the neighboring ripples. Figure 2(d‴) displays a nanobead pattern, clearly showing its 1D nature in a 3D perspective.

The well-defined order of the 1D nanobead pattern of figure 2(d) contrasts strikingly with the relatively poor order of the 2D nanodot pattern of figure 2(e) that forms on an initially flat surface under the same sputtering condition that induces the nanobead pattern on the initially rippled surface. Thus, the ordered growth of the former should originate from the initial condition imposed by the pre-patterned ripples, which limit the kinetic processes randomizing the growth of nanodots and guide their growth along the initial ripples.

Note that Lian *et al* [26] have also reported bead patterns formed by focused-ion-beam irradiation of Co strips and rings formed on silicon oxides, with the lines of beads increasing for wider Co templates. However, in these cases, the bead formation is triggered by dewetting of the Co strips or rings to minimize surface free energy, as a manifestation of the Rayleigh instability [29]. In this case, a well-defined relation between the width of the strip or ring and the period of beads, $\lambda_B > \pi\lambda_R$, is predicted to occur and was actually observed in their experiments. However, such a relation is not met at all for the present case, and the present nanobead formation is, thus, not driven by the Rayleigh instability.

4. Comparison with continuum models

In general, nanoscale pattern formation by IBS has been explained theoretically by continuum models with different levels of sophistication. Note that for the present flux conditions nontrivial morphology changes occur in macroscopic time scales (of the order of seconds) that are not accessible to more atomistic approaches. As mentioned in section 1, a linear model based on Sigmund's theory [15] of ion erosion combined with Mullins's surface-diffusion theory [16] was proposed by Bradley and Harper (BH), and could elucidate the formation of ripples and their orientation with respect to the ion beam [14]. Other features like ripple stabilization are, however, beyond the capabilities of the BH model. To overcome such shortcomings, various nonlinear generalizations have been introduced like the Kuramoto–Sivashinsky (KS) model [30] or the extended KS (eKS) model [31], that were able to reproduce features such as onset of kinetic roughening or ripple coarsening. Besides, the damped KS model [32] has been also suggested to reproduce pattern formation by IBS, although its physical interpretation remains unclear.

Following an alternative route, a 'hydrodynamic' approach [33] to IBS has also led to the eKS model, and could identify local redeposition of sputtered material as the major physical effect behind the improved description of IBS provided by this model. Although the first principles description of IBS is a subject of current debate (see several related papers e.g. in [12]), to date the eKS equation provides a rather complete qualitative description of IBS, that has recently been shown to describe quantitatively experiments on Si targets in a self-consistent fashion [34], and can be expected to apply also to metallic targets. Thus, within this 'hydrodynamical' formulation [2, 33], the dynamics is described both for the surface height $h(\mathbf{r}, t)$ of the target, and for the density $R(\mathbf{r}, t)$ of species (for metals, e.g. adatoms, advacancies [1, 3]) that are subject to transport at the surface and can locally redeposit back to the immobile bulk. In principle, one thus needs to solve a system of two coupled evolution equations. However, due to the smallness of the rate of ion arrival as compared to the rate of atomistic relaxation processes (e.g. surface-diffusion hopping attempts), one can solve approximately the time evolution of $R(\mathbf{r}, t)$ and introduce the result into the equation for $h(\mathbf{r}, t)$, that finally reads [2]

$$\frac{\partial h}{\partial t} = -\nu\nabla^2 h - \mathcal{K}\nabla^4 h + \lambda^{(1)}(\nabla h)^2 + \lambda^{(2)}\nabla^2(\nabla h)^2. \quad (1)$$

In this equation, coefficients ν, $\mathcal{K}$, $\lambda^{(1)}$, and $\lambda^{(2)}$ are functions of phenomenological parameters like the average ion energy and flux, temperature, etc, see [2] and the references therein. In particular, local redeposition induces a non-zero value of coefficient $\lambda^{(2)}$, and contributes additionally to coefficient $\mathcal{K}$. Equation (1) is the eKS model which, after suitable rescaling of h, $\mathbf{r}$ and t, can be expressed as [2]

$$\frac{\partial h}{\partial t} = -\nabla^2 h - \nabla^4 h + (\nabla h)^2 + r\nabla^2(\nabla h)^2 + \eta, \quad (2)$$

where $r = (\nu\lambda^{(2)})/(\mathcal{K}\lambda^{(1)})$ can be interpreted as the ratio of the (squared) nonlinear crossover length scale $|\lambda^{(2)}/\lambda^{(1)}|$

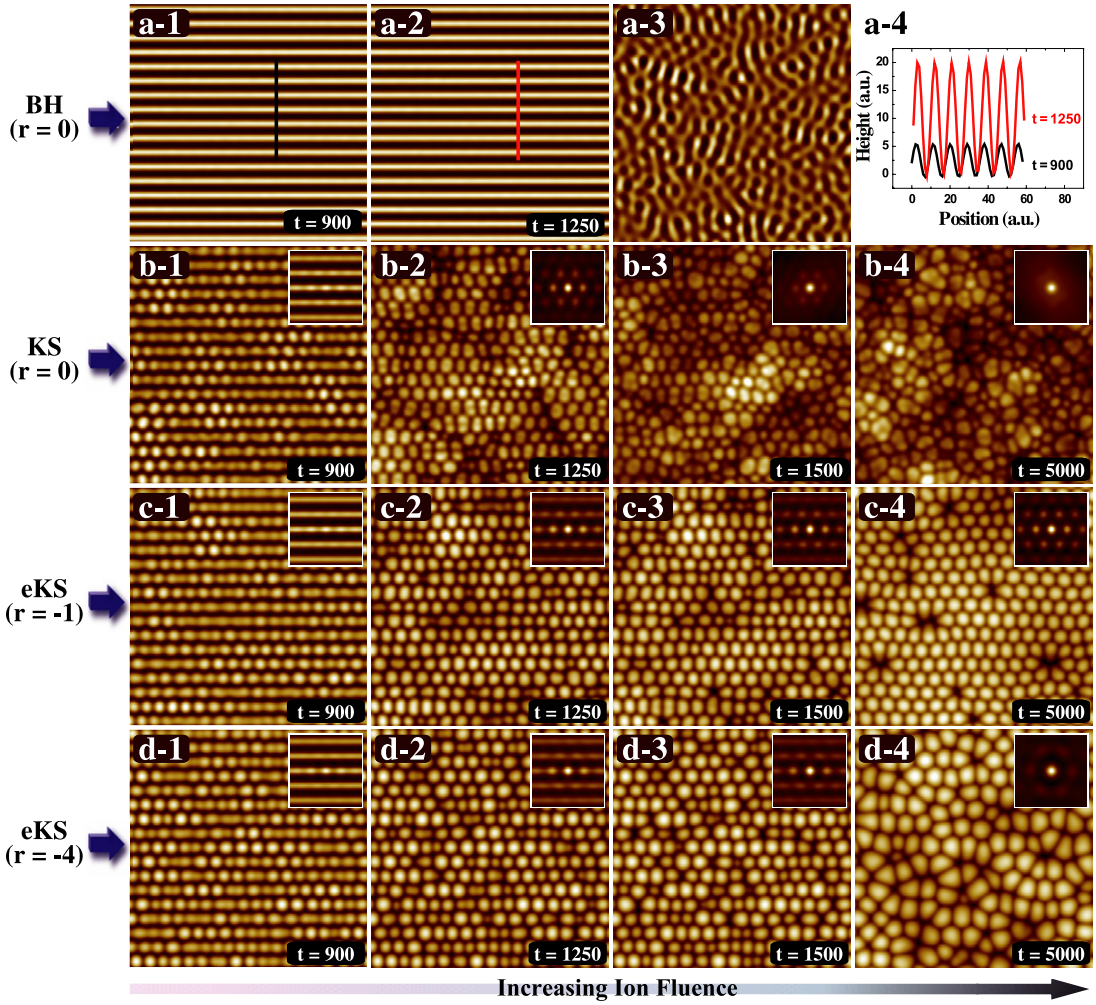

Figure 3. Simulated images at representative simulation times for the (a) BH, (b) KS ($r = 0$), (c) eKS ($r = -1$), and (d) eKS ($r = -4$) models. (a-3) is obtained by differentiating the height of (a-2) along the ripple direction. (a-4) shows the height profiles along the two lines marked respectively in (a-1) and (a-2). Images on the same column are taken at the same simulation times. The simulation time corresponding to each column is also marked with arrows labeled by each column number, from 1 to 4 in figure 4. For the KS ($r = 0$) and the eKS ($r = -1$, -4) models, the images on the left-most column show almost maximal order.

to the (squared) linear crossover length scale $\mathcal{K}/\nu$, and takes negative values for physical conditions [33]. In general, larger r values correspond to conditions under which local redeposition is enhanced leading to stronger coarsening and local ordering properties [2]. The advantage of studying the rescaled equation (2) is that it allows straightforward analysis of the system as a function of the single parameter r on which qualitative properties are thus seen to depend. We have additionally introduced noise fluctuations in equation (2) to account for the randomness of ion arrival, herein described by an uncorrelated, zero-mean Gaussian noise η.

Equation (2) contains both the BH and the KS models as particular cases that are obtained, respectively, by neglecting the two nonlinear terms, or by simply setting $r = 0$. In comparison with these two models, the distinctive feature of the eKS model is the additional presence of the so-called conserved KPZ (cKPZ) nonlinear term with parameter r. As mentioned above, physically it reflects [2, 33] surface-confined transport of species that have been dislodged from the crystalline target but remain on the target surface (local redeposition). Although for semiconductors this mechanism is currently under debate in competition with other relaxation mechanisms such as viscous flow, stress, etc [12] we expect it to be a relevant transport mechanism for metallic surfaces, albeit within a simplified description in which anisotropies to surface diffusion are neglected.

In order to understand how the nanobead patterns' 1D ordering develops and evolves by IBS of rippled surfaces, we perform extensive numerical studies of the relevant models such as the BH, KS, and eKS, trying to assess in particular the relevance of redeposition. Our numerical integration employs centered differences for spatial derivatives, the Euler method for time evolution, and Lam and Shin's [35] discretization for the nonlinear terms.

Figure 3 shows the simulated surface morphologies after IBS normal to the pre-rippled surface according to the (a) BH, (b) KS, (c) and (d) eKS models with $r = -1$ and $r = -4$, respectively. For all cases, the initial ripple wavelengths are chosen to be λ^*, that is, the wavelength of ripples predicted by the linear BH instability.

Figures 3(a-1) and (a-2) are simulated images at two different sputter times according to the BH model, in which no ordered nanobead pattern is observed. Instead, some irregular pattern inscribed on the high rising ripples is revealed in figure 3(a-3), that is obtained by differentiating the height of figure 3(a-2) in the ripple direction, along which the height varies little. Figure 3(a-4) shows profiles along the lines on figures 3(a-1) and (a-2), indicating that just the amplitude of the ripples increases.

For both the KS and eKS models, on the other hand, well-defined nanobead patterns develop by normal IBS of the pre-rippled surfaces. Figure 3(b-1) shows an optimal nanobead pattern for the KS model, and figures 3(c-1) and (d-1) for the eKS model with $r = -1$ and -4, respectively. The height–height correlation maps in their insets show a predominantly 1D order of dots, although a weak, short-range hexagonal order with the beads in the neighboring ripples is also observed. This implies that nonlinear effects are essential for the nanobead formation. Note that in our simulations, the substrate is assumed to be amorphous, while the drive toward close packing of dots dictates their hexagonal order [33, 36]. In our experiments, however, the nanobead patterns reveal a square symmetric order (figure 2). This suggests that the anisotropic diffusion of adspecies via the efficient channels along the ⟨110⟩ directions of crystalline Au(001) plays a significant role for the development of order between the beads in neighboring ripples.

There is, however, a noticeable difference in the temporal evolution of the order upon extended ion-beam sputtering between the KS and the eKS models, namely, further sputtering makes the beads overgrow ripples, and their inter-ripple correlation becomes apparent. (See figures 3(b-2), (c-2), and (d-2).) Still, the 1D order of beads is preserved as shown by the strong intensities of the dots in the central ripple compared with those of the neighboring ripples in the height–height correlation map of each figure. As sputtering proceeds further, the spot intensities in the height–height correlation maps in figures 3(b-3), (c-3), and (d-3) becomes weak with respect to the central spot, indicating that the spatial order of the beads becomes weak. For the KS model, the 1D order is already obscure in figure 3(b-3), while it is still well discernable for the eKS model. With further sputtering, the spatial order of dots becomes poorer. (See figures 3(b-4), (c-4), and (d-4).) Even no orientational order of dots is observed for the KS model as seen in the height–height correlation map in figure 3(b-4). For the eKS model, the temporal evolution of order changes, depending on the relative strength of r. With $r = -4$, the order of dots looks 2D like as noticed from the inset of figure 3(d-4), while for $r = -1$, the 1D order of dots is still well preserved. Thus, there seems to be an optimal strength (r value) of the cKPZ term for nanobead pattern enhancement.

In order to perform a semi-quantitative analysis of the temporal evolution of the 1D order in the nanobead pattern, we choose to define an ordering parameter as the intensity of the first order peak relative to that of the zeroth order peak along the central ripple of the height–height correlation map of the nanobead pattern. In figure 4, the temporal evolution of the ordering parameter is displayed for the simulated

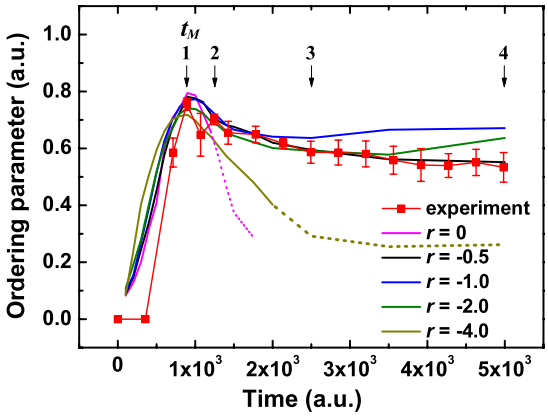

Figure 4. Temporal evolution of the ordering parameter for the experimental and simulated nanobead patterns for r values from 0 to -4. The relative intensity of the first order peak to that of the zeroth order peak along the central ripple on the 2D height–height correlation map is taken as the ordering parameter. Solid (dashed) lines denote the case where a well-defined nanobead pattern (poor or 2D like) forms. The simulation time is scaled to the experimental ion fluence so as to synchronize the time showing the maximum ordering parameter. Each arrow on the upper side of the figure that is labeled by a number denotes the simulation time of the images in the corresponding numbered columns in figure 3.

nanobead patterns for various r from 0 to -4, along with the experimental ones. The wavelength of the pre-patterned ripple is chosen to be λ^*. For all the simulations, the ordering parameters show maxima around $t_M = 900$ in simulation units. As noticed in figure 3, there is a difference in the temporal evolution of the ordering parameter between the KS and the eKS models. For the KS model ($r = 0$), the ordering parameter degrades very rapidly, as compared with the cases in which r is not zero (eKS model). For $r = -0.5$, -1, and -2, the 1D order of the nanobead pattern is preserved for quite a long time. For $r = -4$, however, the 1D order is lost at a relatively early time.

The experimentally observed ordering parameter is also displayed in figure 4 after rescaling the experimental time and magnitude of the ordering parameter, so that it shows its maximum at the same time and with the same magnitude as the mean theoretical ones. After reaching maximum, the experimentally observed ordering parameter decreases slightly, and then remains high for a long time, seemingly being at a stationary state. All these details are well reproduced by the eKS model, especially with $r = -0.5$ in figure 4. Thus, as in the case of Si targets [34], the eKS model seems a self-consistent model to reproduce the intricate temporal evolution of nanobead patterns, even at a semi-quantitative level.

As mentioned above, the cKPZ nonlinearity appearing in the eKS model represents local redeposition effects [33] that appear to be essential in order to heal the ion-eroded surface, seeming to preserve the ordering parameter as observed in figure 4. In analogy with the pattern formation in macroscopic systems such as ripples on sand dunes, the surface-confined transport of redeposited material tends to promote lateral coarsening of the pattern features, which is more pronounced for large r values [2]. In our case, this effect competes

with alignment of the nanobeads along the original ripples on the target, there being an optimal balance at $r = -0.5$ between both trends that provides an arrangement with the best ordering. For instance, for $r = -4$ in figure 3(d-4) it is apparent that coarsening of the individual beads up to a larger stationary lateral size hinders 1D bead alignment. Actually, we also observe in our experimental study on the initial wavelength dependence of the nanobead pattern that the well-defined, stable nanobead pattern forms when the ripple wavelengths are comparable with the diameter of the nanobeads [28].

In short, we find that most of the experimental observations such as the formation of a bead pattern and the temporal evolution of its 1D order are reproduced solely by eKS model. This indicates that nonlinear effects such as local redeposition and surface-confined transport represented by cKPZ term in the model are significant for the formation and preservation of the nanobead pattern. The simulation shows the hexagonal order of the beads in the neighboring ripples that are contrasted with the square symmetry of the beads observed in experiments. This originates from the fact that the model assumes an isotropic surface.

5. Summary and conclusions

In summary, by introducing a two-step process (sequential-ion-beam sputtering) that combines a suitable pre-patterned target with subsequent irradiation at normal incidence, we have been able to fabricate by IBS a novel nanobead pattern on Au(001). This demonstrates the capability of IBS for hierarchical self-assembly of sophisticated nanostructures that is moreover achieved via a fully bottom-up approach. As expected on general grounds, in our system the IBS morphological instability leads to a disordered dot pattern when starting out from a flat initial condition. However, we have seen that the choice of an initial rippled surface is able to guide the one-dimensional alignment of the dots, ending up in the nanobead morphology that had not been reported in this context as yet. Actually, comparison with continuum models has allowed us to illustrate the dependence of the quality of the nanobead pattern (in terms of one-dimensional order, i.e., length of uninterrupted 'chains' of dots and side-by-side arrangement of such chains) on the features of both the initial condition [28] and on the parameters that characterize the chosen experimental conditions (ion incidence angle and average energy, ion-target species combination, etc). Thus, for a fixed choice of the latter as in our experiment, different initial conditions lead to different ordering properties: a flat initial condition (that one could think of as a rippled surface with a wavelength much larger than any other length scale in the system) gives a disordered dot pattern, while a rippled initial condition whose typical scale is comparable to the dot size leads to dot alignment [28]. Conversely, we have seen that changes in experimental parameters also induce changes in the quality of the nanobead pattern, there being an optimum parameter choice that in our experiments corresponds to the results that we have reported.

Considering the universal character of nanopatterning by IBS, the present scheme of hierarchical self-assembly should be transferable to most other materials, and is expected to open a new avenue for this technique. In particular, while in our case we have demonstrated nanobead production on a metallic target, the comparison that we have presented with continuum models specifically suggests that a similar hierarchical pattern could be produced on semiconducting targets for appropriate incidence geometries. Note that the latter type of target becomes amorphous under the type of IBS conditions that we have considered [37], so that surface transport (e.g. surface diffusion) is properly isotropic, precisely as assumed in the models discussed in section 4. Regarding these, we have seen in particular that the eKS model self-consistently reproduces most of the experimental details for the formation of the nanobead patterns in contrast with other available models. Given that the role of local redeposition and surface-confined transport is a distinctive feature of this model in comparison with the other models considered in section 4, we can conclude on the importance of these relaxation processes for the present type of nanoscopic pattern formation systems. Naturally, improvements in the quantitative continuum description of the present experiments might be expected from a more detailed description that takes into account anisotropies in surface diffusion that are typical of metallic substrates and have been neglected here.

About specific applications of the present nanobead pattern, note that the well-known ripple patterns that are produced by IBS have already shown a variety of optical and catalytic properties that differ from those of their bulk states due to their corrugated structures at the nanoscale [8, 38, 39]. Such patterns have also been used for templates for magnetic nanostructures that showed modified interesting magnetic properties such as magnetic anisotropy [9]. The nanobead pattern that we have produced can be applied to the above mentioned areas as well, and is expected to show salient properties due to its intricate structure. Furthermore, it has a great potential to be applied for optically functional devices using surface plasmon resonance, and also for the study of surface enhanced Raman spectroscopy [40, 41].

Acknowledgments

The work was supported by NRF (Korea) Grant Nos 20100010481 and 20110015308, and by MICINN (Spain) Grant No. FIS2009-12964-C05-01. R C gratefully acknowledges warm hospitality at Sook-Myung Women's University while part of this work was done.

References

[1] Chan W L and Chason E 2007 *J. Appl. Phys.* **101** 121301
[2] Muñoz-García J, Vázquez L, Cuerno R, Sánchez-García J A, Castro M and Gago R 2009 Self-organized surface nanopatterning by ion beam sputtering *Towards Functional Nanomaterials* ed Z M Wang (New York: Springer)
[3] Valbusa U, Boragno C and de Mongeot F B 2002 *J. Phys.: Condens. Matter* **14** 8153

[4] Facsko S, Dekorsy T, Koerdt C, Trappe C, Kurz H, Vogt A and Hartnagel H L 1999 *Science* **285** 1551
[5] Lu M, Yang X J, Perry S S and Rabalais J W 2002 *Appl. Phys. Lett.* **80** 2096
[6] Wei Q, Lian J, Zhu S, Li W, Sun K and Wang L 2008 *Chem. Phys. Lett.* **452** 124
[7] Moon M W, Lee S H, Sun J Y, Oh K H, Vaziri A and Hutchinson J W 2007 *Proc. Natl Acad. Sci. USA* **104** 1130
[8] Costantini G, Buatier de Mongeot F, Rusponi S, Boragno C, Valbusa U, Vattuone L, Burghaus U, Savio L and Rocca M 2000 *J. Chem. Phys.* **112** 6840
[9] Moroni R, Sekiba D, de Mongeot F B, Gonella G, Boragno C, Mattera L and Valbusa U 2003 *Phys. Rev. Lett.* **91** 167207
[10] Fassbender J, Strache T, Liedke M O, Markó D, Wintz S, Lenz K, Keller A, Facsko S, Mönch I and McCord J 2009 *New J. Phys.* **11** 125002
[11] Everts F, Wormeester H and Poelsema B 2008 *Phys. Rev.* B **78** 155419
[12] Cuerno R, Vázquez L, Gago R and Castro M (guest editors) 2009 *J. Phys.: Condens. Matter* **21** (issue 22, special section Surface nanopatterns induced by ion-beam sputtering)
[13] Cross M and Greenside H 2009 *Pattern Formation and Dynamicsin Nonequilibrium Systems* (Cambridge: Cambridge University Press)
[14] Bradley R M and Harper J M E 1988 *J. Vac. Sci. Technol.* A **6** 2390
[15] Sigmund P 1969 *Phys. Rev.* **184** 383
[16] Mullins W W 1959 *J. Appl. Phys.* **30** 77
[17] Frost F, Schindler A and Bigl F 2000 *Phys. Rev. Lett.* **85** 4116
[18] Ziberi B, Frost F, Tartz M, Neumann H and Rauschenbach B 2008 *Appl. Phys. Lett.* **92** 063102
[19] Carter G 2004 *Vacuum* **77** 97
[20] Carter G 2005 *Vacuum* **79** 106
[21] Vogel S and Linz S J 2007 *Phys. Rev.* B **75** 085425
[22] Joe M, Choi C, Kahng B and Kim J-S 2007 *Appl. Phys. Lett.* **91** 233115
[23] Kim J-H, Joe M, Kim S-P, Ha N-B, Lee K-R, Kahng B and Kim J-S 2009 *Phys. Rev.* B **79** 205403
[24] Keller A and Facsko S 2010 *Phys. Rev.* B **82** 155444
[25] Cuenat A, George H B, Chang K-C, Blakely J M and Aziz M J 2005 *Adv. Mater.* **17** 2845
[26] Lian J, Wang L, Sun X, Yu Q and Ewing R C 2006 *Nano Lett.* **6** 1047
[27] Kim T C, Jo M H, Kim Y, Noh D Y, Kahng B and Kim J-S 2006 *Phys. Rev.* B **73** 125425
[28] Kim J-H, Kim J-S and Cuerno R 2011 at press
[29] Nichols F A and Mullins W W 1965 *Trans. Metall. Soc. AIME* **233** 1840
[30] Makeev M A, Cuerno R and Barabási A-L 2002 *Nucl. Instrum. Methods Phys. Res.* B **197** 185
[31] Kim T C *et al* 2004 *Phys. Rev. Lett.* **92** 246104
[32] Facsko S, Bobek T, Stahl A, Kurz H and Dekorsy T 2004 *Phys. Rev.* B **69** 153412
[33] Castro M, Cuerno R, Vázquez L and Gago R 2005 *Phys. Rev. Lett.* **94** 016102
[34] Muñoz-García J, Gago R, Vázquez L, Sánchez-García J A and Cuerno R 2010 *Phys. Rev. Lett.* **104** 026101
[35] Lam C-H and Shin F G 1998 *Phys. Rev.* E **58** 5592
[36] Facsko S, Kurz H and Dekorsy T 2001 *Phys. Rev.* B **63** 165329
[37] Gnaser H 1998 *Low Energy Ion Irradiation of Solid Surfaces* (New York: Springer)
[38] Belardini A, Larciprete M C, Centini M, Fazio E, Sibilia C, Bertolotti M, Toma A, Chiappe D and de Mongeot F B 2009 *Opt. Express* **17** 3603
[39] Toma A, Chiappe D, Boragno C and de Mongeot F B 2010 *Phys. Rev.* B **81** 165436
[40] Oates T W H, Keller A, Facsko S and Mücklich A 2007 *Plasmonics* **2** 47
[41] Camelio S, Babonneau D, Lantiat D, Simonot L and Pailloux F 2009 *Phys. Rev.* B **80** 155434